Nuclear Instruments and Methods in Physics Research A 1064 (2024) 169470

Contents lists available at ScienceDirect

Nuclear Inst. and Methods in Physics Research, A

journal homepage: www.elsevier.com/locate/nima

High-speed continuous X-ray imaging method based on SiPM auto-encoding detector

Xuemei Lyu [a], Pin Gong [a,b,*], Zhimeng Hu [a,b], Cheng Zhou [c], Xiaoxiang Zhu [c], Xiaobin Tang [a,b,**]

[a] Department of Nuclear Science and Technology, Nanjing University of Aeronautics and Astronautics, Nanjing, 210016, China
[b] Key Laboratory of Nuclear Technology Application and Radiation Protection in Astronautics, Ministry of Industry and Information Technology, Nanjing University of Aeronautics and Astronautics, Nanjing, 210016, China
[c] Jiangsu Nuclear and Radiation Safety Supervision and Management Center, Nanjing, 210019, China

ARTICLE INFO

Keywords:
Silicon photomultiplier
Autoencoder
High-speed X-ray imaging

ABSTRACT

High-speed X-ray imaging can be used to observe the internal evolution of objects in the microsecond range. However, obtaining data and processing images continuously are difficult when the speed of X-ray imaging is more than one million frames per second (fps). The novel method of high-speed X-ray imaging, which is based on a SiPM auto-encoding detector, was proposed. The different response to X-ray is realized by adjusting the bias voltage of different pixels to encode the analog signals. The analog signals from multiple SiPM pixels are simplified into a single signal. In this way, SiPM is constructed as the SiPM auto-encoding detector, which greatly reduces the amount of analog signals to be sampled for each frame of X-ray image, and then the image is reconstructed in the upper computer. The feasibility of the imaging method was verified by coupling the pixelated SiPM and lutetium-ytterbium scintillation crystals to construct a SiPM auto-encoding detector. Six patterns were exposed when pulsed X-rays were performed at frequencies of 100 and 500 kHz. Then, the number of image pixels was compressed from 16 to 4. The peak signal-to-noise ratio of the reconstructed images was above 41, and the structural similarity was above 0.99. Experimental results demonstrated that the speed of continuous X-ray imaging reached 500, 000 fps for six kinds of 4×4 pixel patterns. This method can be applied to improve the speed of high-speed continuous X-ray imaging.

1. Introduction

High-speed X-ray imaging has been widely applied to capture dynamic processes, such as additive manufacturing [1,2], battery thermal runaway [3], ballistic impacts [4], crack propagation, and arc ignition [5]. Continuous real-time monitoring is required in laser processing to determine the size and location of pores in the material [6,7]. A high-speed camera coupled scintillator is mainly used for high-speed X-ray imaging with an imaging time between microseconds and milliseconds [8]. The speed of imaging has been primarily improved through a scintillator with faster decay time [9], pixel array detectors (PADs) with faster imaging speeds [10], fast digital readout [11,12], and FPGA acceleration [13,14]. High-speed X-ray imaging could be performed on the nanosecond scale, but doing so is suitable for limited frames operating in continuous mode [15] mainly because it takes a much longer time to read out offline.

At present, the speed of high-speed continuous X-ray imaging is on the tens of microseconds, which mainly depends on the speed of signal readout [16]. The signals generated by the X-ray detector increase with the number of detector pixels. If X-ray imaging is to be performed continuously, then the readout of signals must be completed within the interval of two pulsed X-ray beams. The ADC requires a large number of parallel channels to convert analog signals. Even in-pixel ADCs have been developed [17], but bottlenecks in high-speed off-chip data transfer remain. A detector operating at tens to hundreds of kilohertz with millions of pixels generates 10^{12} bits per second if every analog signal converts to 10-bit data words. However, it is not feasible for system integration to parallel hundreds of off-chip ASICs. On-chip data compression provides an effective solution that is expected to realize high frame rate of 1 Mfps without deadtime, but it is limited by ADCs [18].

In this study, the analog signals of multiple pixels are simplified into

* Corresponding author. Department of Nuclear Science and Technology, Nanjing University of Aeronautics and Astronautics, Nanjing, 210016, China.
** Corresponding author. Department of Nuclear Science and Technology, Nanjing University of Aeronautics and Astronautics, Nanjing, 210016, China.
E-mail address: gongpin@nuaa.edu.cn (P. Gong).

https://doi.org/10.1016/j.nima.2024.169470
Received 13 November 2023; Received in revised form 5 February 2024; Accepted 21 May 2024
Available online 22 May 2024

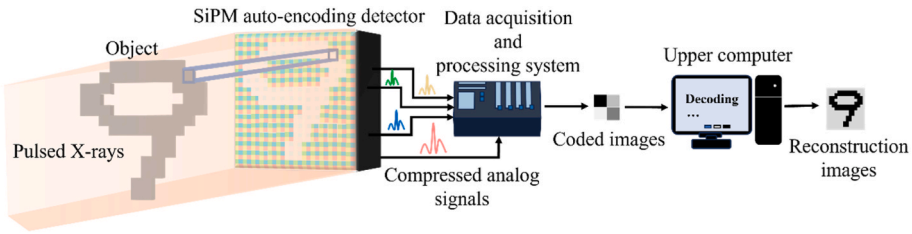

Fig. 1. Procedure of high-speed continuous X-ray imaging with SiPM auto-encoding detector. After penetrating an object, pulsed X-rays are sensed by the SiPM auto-encoding detector, and the analog signals of images are compressed. The compressed analog signals are further converted to coded images by the data acquisition and processing system, and the coded images are reconstructed in the upper computer.

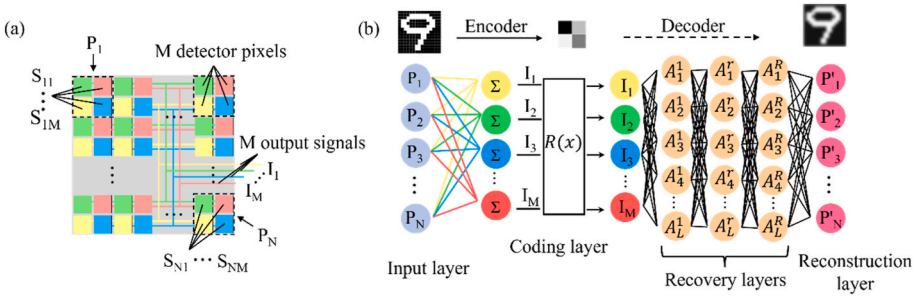

Fig. 2. Schematic of SiPM auto-encoding detector. (a) Structure of SiPM auto-encoding detector array. An image pixel P consists of M detector pixels S. Signals from detector pixels with same color are connected in parallel to form the output signal I, and there are M output signals. (b) Architecture of autoencoder. Above the autoencoder, an example of encoding and decoding is shown. The original image from the MNIST handwritten dataset is encoded into four coding layer neurons and then decoded into an image similar to the original image. The encoder includes an input layer and a coding layer. The decoder includes R layers of recovery layer and one layer of reconstruction layer.

one to reduce the amount of transferred data, and a silicon photomultiplier (SiPM) is used to prove the effectiveness of the method. The pixelated SiPM was coupled with a scintillator to form a radiation detector for X-ray imaging. The analog signals were successfully compressed by setting an artificial neural network in the detector array. The images can be restored through reconstruction. This method is first proved to be practicable in high-speed continuous X-ray imaging.

2. Principle

The imaging approach is described in detail in Fig. 1. The SiPM coupled scintillator is utilized to construct the SiPM auto-encoding detector. The procedure of high-speed continuous X-ray imaging is shown in Fig. 1. When the pulsed X-rays penetrate an object, the SiPM auto-encoding detector converts X-ray signals into compressed analog signals. The data acquisition and processing system collects the signals to obtain coded images. In the upper computer, the images of the object are reconstructed by decoding. The transient evolution can be observed by continuously imaging with high-frequency pulsed X-rays.

The structure of the SiPM auto-encoding detector is illustrated in Fig. 2(a). The detector has N × M pixel; every detector pixel is called S. An image pixel P consists of M detector pixels. Therefore, a total of N image pixels are present. Fig. 2(b) shows the architecture of the autoencoder. An autoencoder is a neural network consisting of two parts: an encoder and a decoder. Every layer is fully connected. The encoder consists of two layers: (1) an input layer with N neurons and (2) a coding layer with M neurons. The activation function of the coding layer is

$$R(x) = \max(0, x). \tag{1}$$

The output of coding layer is given by

$$I = R(W_e P + b_e), \tag{2}$$

where W_e is the weight matrix of the encoder, with the number of weights being the same as the number of detector pixels, and b_e denotes the bias vector. The weights of the encoder are all positive to ensure compatibility with the detector. The coding layer has no bias terms. Correspondingly, M output current channels are present in the detector array to equal with the neurons of the coding layer. In the detector array, paralleling the output signals of S with the same color according to Kirchhoff's law, the output current signal I can be analogous to the summation process of the network. The analog signals from multiple SiPM pixels are simplified into a single signal in this way. Therefore, mapping the weights of encoder to the detector array can set the encoder in Fig. 2(b) in the detector array to complete the construction of the SiPM auto-encoding detector.

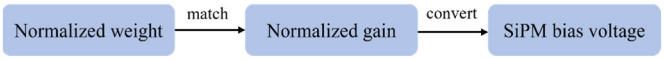

Fig. 3. Establishment of the relationship between weight of the encoder and SiPMs' bias voltage.

A SiPM consists of multiple avalanche photodiodes, and its output signal amplitude is influenced by its bias voltage [19]. For a given input, a higher bias voltage corresponds to a higher gain, resulting in a larger amplitude of output signal. X-rays are converted into optical light of a specific wavelength by the scintillator, and then the current is generated by SiPM. Setting the bias voltage of each SiPM pixel individually can produce current signals with different amplitudes if the input remains the same. Therefore, we can establish the corresponding relationship between SiPM bias and the weights of the encoder. According to the official datasheet of SiPM, a linear relationship exists between the gain and the bias between 52 and 60 V. As shown in Fig. 3, the normalized weight is matched with the normalized gain to set the bias voltage of each pixel of SiPM.

The output of the encoder needs to be recovered by the decoder. As shown in Fig. 2(b), the decoder consists of two layers: (1) recovery layers with L neurons per layer, especially, L = 1.5 N, and (2) a reconstruction

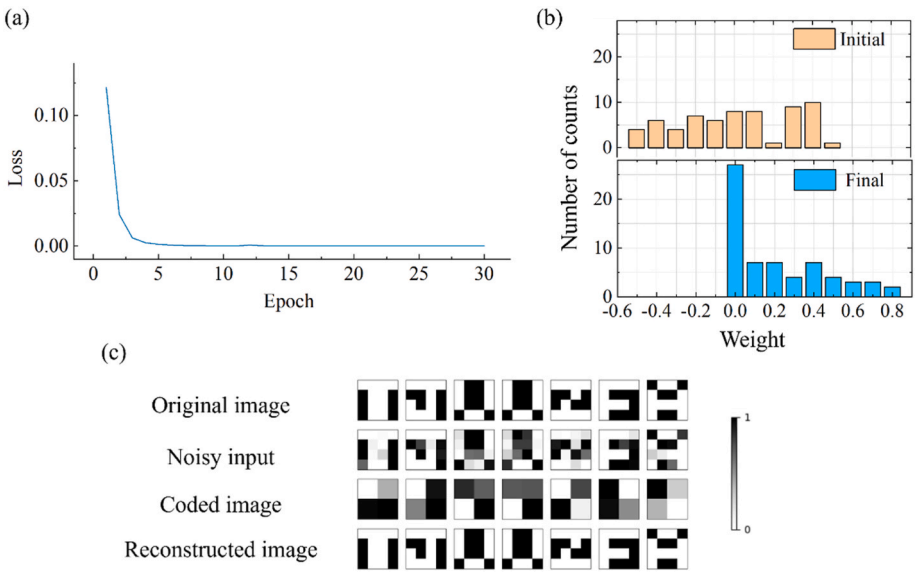

Fig. 4. Training results of autoencoder. (a) Loss of the autoencoder during training. (b) Weights of the encoder before and after training. (c) Some test images were reconstructed by the decoder. The image with noise was compressed by the encoder and restored by the decoder.

layer with N neurons. Each recovery layer is followed by a tangent activation function defined as

$$T(x) = \{\exp(x) - \exp(-x)\}/\{\exp(x) + \exp(-x)\}. \quad (3)$$

Therefore, given the weight matrix W_r and the bias vector b_r, the activation of the r-th recovery layer is given by

$$A_r = T(W_r A_{r-1} + b_r), \quad (4)$$

where $r = 1, \ldots, R$. The activation function of the reconstruction layer is defined as

$$S(x) = 1/\{1 + \exp(-x)\}. \quad (5)$$

The output of the reconstruction layer is given by

$$P' = S(W_d A_R + b_d), \quad (6)$$

where W_d is the weight matrix between the R-th recovery layer and the reconstruction layer, and b_d denotes the bias vector of the reconstruction layer. The autoencoder was trained with an adaptive moment estimation (Adam) optimizer [20] and the mean square error loss function,

$$\zeta = \left\{ \sum_{i=1}^{N} (P_i - P_i')^2 \right\} \Big/ N. \quad (7)$$

The loss depends on the difference between the original and reconstructed images. Once the training is complete, the encoder and the decoder are fixed and saved into files, which can be easily loaded and used.

3. Training of autoencoder

To verify the method, we first trained a concrete autoencoder. N, M, L, and R were 16, 4, 24, and 3, respectively. The input to this network was noisy images, including the letters A, F, J, T, V, and Z. The bright and dark levels were the same as in the original image. The Gaussian noise and crosstalk noise that would be generated in the actual process were considered to ensure that the training is close to the real situation. With a noise level of 0.2, 900 input images (150 images per letter) were split into two categories: train and test (80 and 20, respectively). The original images were employed as the label.

As depicted in Fig. 4(a), the autoencoder was trained for 30 epochs. From the curve, the loss decreased steeply in the first ~3 training

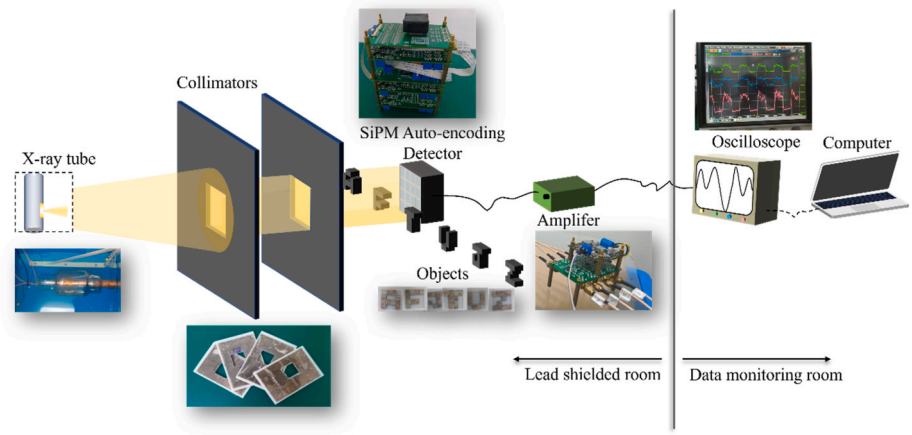

Fig. 5. Experimental setup of high-speed continuous X-ray imaging based on SiPM auto-encoding detector. The X-ray tube was immersed in insulating oil to create a vacuum environment. Except for the oscilloscope and the computer, other components were in a lead-shielded room.

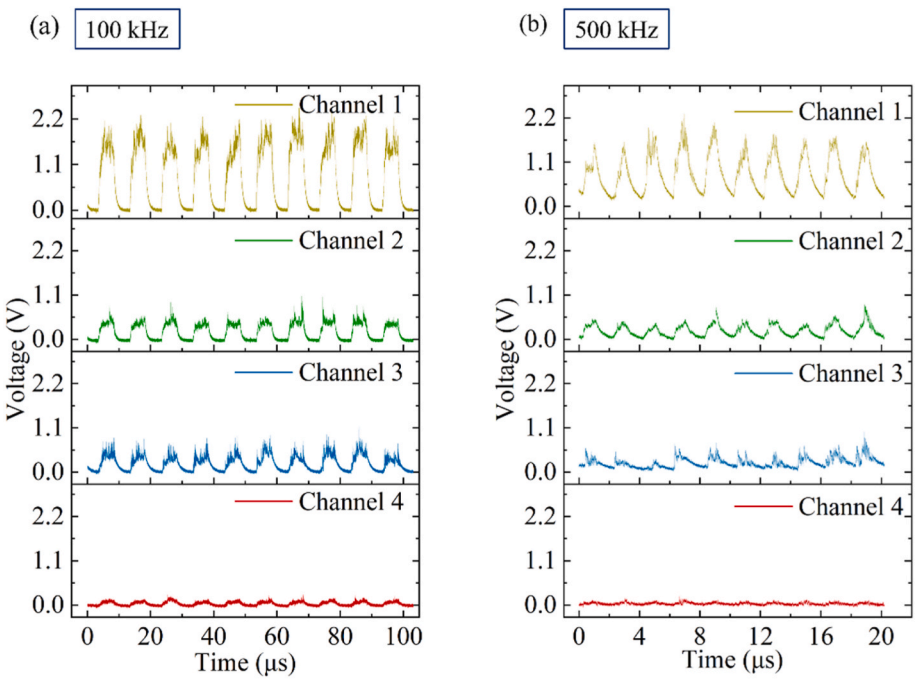

Fig. 6. Waveforms of compressed signals. (a) Compressed signals at 100 kHz. (b) Compressed signals at 500 kHz.

epochs. After about 10 epochs, the loss slowly converged to a final value, with little fluctuation. The initial and final weights of the encoder can be seen in Fig. 4(b); the weights were not less than 0 after training, and the values were between 0 and 1. Fig. 4(c) shows the reconstruction performance of the decoder. The original image with noise was compressed by the encoder. Each image is compressed into a unique coded image. The coded images maintained a similar brightness distribution for the same original image. Slight differences occurred because of the noise. Every image was clearly restored without noise by the decoder. This finding shows that the images in the training database can be efficiently compressed by the encoder and clearly reconstructed by the decoder. Then, the weights of the encoder were mapped to the detector array, and the decoder was used to reconstruct coded images output by the SiPM auto-encoding detector during the subsequent experiment.

4. Experiment

4.1. Experimental setup

Once the SiPM auto-encoding detector and the decoder were ready, the actual experimental effect can be tested. As shown in Fig. 5, the experiment used a grid-controlled modulated X-ray tube developed by our laboratory, which can generate stable pulsed X-rays with frequencies from 1 kHz to 1 MHz [21]. The emitted X-ray energy from this tube was mainly distributed around 10 keV at 50 kV tube voltage. Two-layer collimators made of lead were arranged at a distance of 30 cm from the X-ray source to obtain a parallel X-ray beam due to the absence of additional focusing structures on the detector. The thickness of each collimator was 1 mm, and the distance between them was 3 cm. The size of the collimation hole was 25 mm × 25 mm, which was the same as the size of the objects and the detector. After passing through the collimators, pulsed X-ray reached the object through 2 cm of air. The patterns were the same as the autoencoder-trained images in Fig. 4(c), containing the letters A, F, J, T, V, and Z. They were spliced by tungsten blocks, which were placed 1 cm in front of the detection array. The size of each tungsten block was 3 mm × 3 mm × 1 mm. LYSO crystal with fast luminescence decay time (about 43 ns) and high light yield (about 70% relative to NaI) was selected to ensure the speed of continuous X-ray imaging. The overall crystal size was 25 mm × 25 mm × 10 mm, which was consistent with the coupled SiPM array, and it was divided into uniform 8 × 8 pixel. The size of each pixel was 3 mm × 3 mm with a 0.2 mm BaSO4 reflective layer between pixels. This crystal was combined with 8 × 8 pixel SiPM by an optical couplant. The SiPM was one of the series of products produced by Hamamatsu with low crosstalk and dark counts. The photosensitive area of each pixel was 3 mm × 3 mm. The pixels of SiPM were connected into four output channels, as illustrated in Fig. 2(a). Then, the four compressed current signals were linearly amplified by a high-speed amplifier, and the signals were connected to an oscilloscope for observation or storage.

4.2. Encoding stability

When the frequency of pulsed X-ray was 100 and 500 kHz, compressed signals of the same pattern were collected for 10 consecutive periods. Observing the waveform of compressed signals is a suitable way to analyze the encoding stability. Fig. 6(a) shows the compressed signals at 100 kHz. The four compressed signals are represented by four colored lines of yellow, green, blue, and red, respectively. The ordinate was voltage because we used an amplifier and observed them on an oscilloscope, which made an I–V conversion process. The compressed signals were periodic, and their changing frequency was the same as that of pulsed X-ray. The signals were relatively stable, thereby indicating that the signals produced by a single pulsed X-ray beam can be isolated and transmitted continuously by the system. The compressed signals at 500 kHz are shown in Fig. 6(b), which had 10 periods. As a result of the fixed sampling rate, the data points were sparse at 500 kHz, and the waveform still fluctuated periodically. Every period was about 2 μs. A 500 kfps continuous readout for a 4 × 4 pixel image can be achieved with four channels in parallel [22]. Compared with the signals at a waveform of 100 kHz, the signals were a little bit distorted, and the amplitude decreased because a high X-ray frequency meant fewer X-rays in every period. Thus, the number of photons entering each pixel will exhibit a large statistical fluctuation, and this fluctuation will lead to the failure of encoding so that the image cannot be reconstructed correctly.

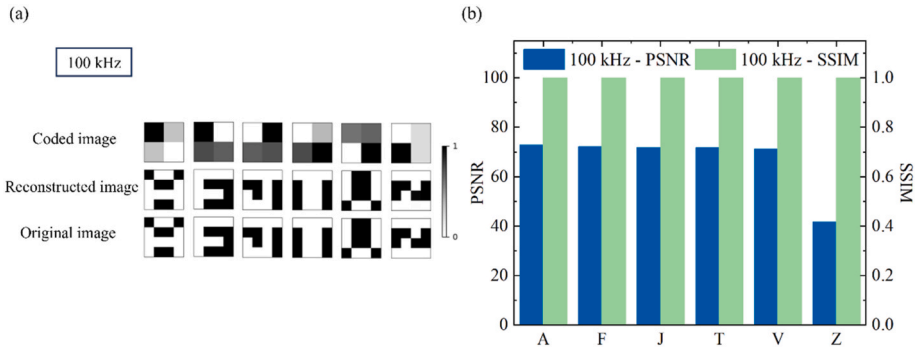

Fig. 7. Imaging results at 100 kHz. (a) When the frequency of pulsed X-rays was 100 kHz, the SiPM auto-encoding detector translated the projected images into compressed signals, and then the signals were converted into coded images and finally reconstructed into an image by the decoder. (b) PSNRs and SSIMs of reconstructed images at 100 kHz.

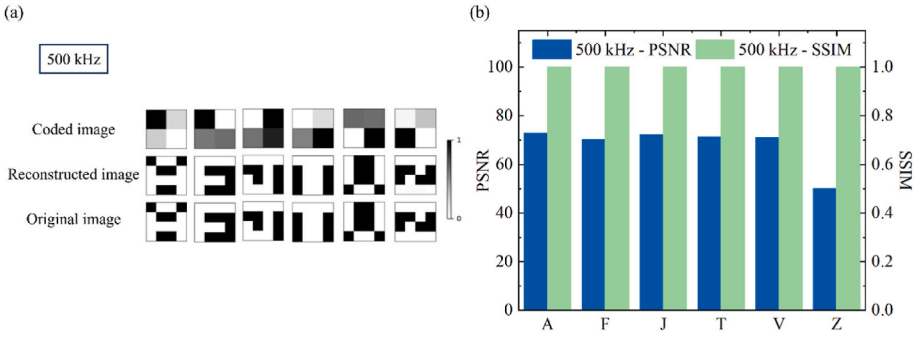

Fig. 8. Imaging results at 500 kHz. (a) When the frequency of pulsed X-rays was 500 kHz, the SiPM auto-encoding detector translated the projected images into compressed signals, and then the signals were converted into coded images and finally reconstructed into an image by the decoder. (b) PSNRs and SSIMs of reconstructed images at 500 kHz.

4.3. Reconstruction results of coded images

The SiPM auto-encoding detector was operated as an encoder to compress the patterns. Compressed signals of six letters in one period were collected for reconstruction under the pulsed X-ray of two frequencies to verify that the method can be used for X-ray imaging. One-dimensional array was obtained by sequentially collecting the amplitude of compressed signals, which was viewed as the output of the encoder. Then, it was converted into a 2×2 array to obtain the coded image. During reconstruction, 16 outputs were obtained by inputting the one-dimensional array into the decoder in the upper computer, and the reconstructed image could be obtained by transforming the outputs into a 4×4 array. The speed of X-ray imaging is not less than $1/T$, where T is the period of pulsed X-rays. The peak signal-to-noise ratios (PSNRs) and structural similarities (SSIMs) were used to evaluate the reconstruction performance. If the PSNR is higher, then the reconstruction is better. The closer the SSIM is to 1, the more similar the reconstructed image is to the original image.

As can be seen from Fig. 7(a), each projected letter at 100 kHz delivered a unique coded image at the output. The reconstructed image correctly corresponded to the original image, and the reconstructions were considerably less noisy. The PSNRs and SSIMs of reconstructed images could be seen in Fig. 7(b). The reconstruction performance at 100 kHz was good, which indicated that the speed of continuous X-ray imaging can reach 100 kfps for six letters. For the reconstructed images, the PSNRs of letters A, F, J, T, and V were all above 70, and the PSNR of letter Z was 41.73, which was not as good as that of the other letters. The SSIMs of all six letters remained at 0.99. The X-rays produced by the X-ray tube show a certain spatial distribution. Although the collimators can minimize the dispersion of the X-rays as much as possible, scattered X-rays inevitably exist. Scintillators convert the X-rays into optical light. When optical light passes through the coupling interface between the scintillator and SiPM, reflection and refraction slightly lead to optical crosstalk. These factors cause errors in the amount of incident optical light in some pixels of SiPM, resulting in the reduction in the PSNR of letter Z. Some electronic noises can also affect the reconstruction. Electromagnetic interference will cause waveform oscillation, which will affect the judgment of signal amplitude, thus leading to image reconstruction failure.

Similarly, as can be seen in Fig. 8(a), at 500 kHz, different letters were compressed into different coded images. For the same letter, the coded images were consistent with that at 100 kHz. The coded image of the letter Z was different from that of 100 kHz, and this difference could not affect its reconstruction. This result illustrated the fault tolerance of the decoder. For six letters, the PSNRs and SSIMs in Fig. 8(b) showed that the overall reconstruction performance was also good, which indicated that the speed of continuous X-ray imaging can reach 500,000 fps at least. For the reconstructed images, the PSNRs of letters A, F, J, T, and V were all above 70. The PSNR of letter Z was also not as good as that of the other letters, and the SSIMs of all six letters still remained at 0.99. For letter Z, the coded images had a minimal difference at the two frequencies. This situation did not appear in other patterns. Therefore, the arrangement of letter Z may be a non-negligible factor except for other experimental factors.

5. Conclusion

In this study, a new high-speed continuous X-ray imaging method was proposed. This method can reduce the number of analog signals that need to be sampled without delay. In this way, the speed of high-speed continuous X-ray imaging is expected to be improved. The autoencoder was trained offline and saved into files for experiment. During the

experiment, six letters were projected by pulsed X-ray, and 16 image pixels were compressed into 4 pixels in the analog domain. The correct pattern can be reconstructed by the decoder in the upper computer. The PSNRs and SSIMs were above 41 and 0.99, respectively, indicating that the speed of continuous X-ray imaging reached 500, 000 fps for six letters. According to the compression scheme in the experiment, the amount of data is reduced to one-fourth of the original. Although the patterns are relatively simple, it is enough to prove that this method can compress image analog signals for high-speed continuous X-ray imaging. For more image pixels, the SiPM auto-encoding detector can reach a larger compression ratio. However, a large compression ratio means a great difference between the reconstructed image and the original image.

CRediT authorship contribution statement

Xuemei Lyu: Conceptualization, Data curation, Formal analysis, Investigation, Methodology, Resources, Software, Writing – original draft, Writing – review & editing. **Pin Gong:** Funding acquisition, Supervision, Writing – review & editing, Conceptualization, Methodology. **Zhimeng Hu:** Funding acquisition, Supervision. **Cheng Zhou:** Supervision. **Xiaoxiang Zhu:** Supervision. **Xiaobin Tang:** Funding acquisition, Supervision, Writing – review & editing.

Declaration of competing interest

The authors declare that they have no known competing financial interests or personal relationships that could have appeared to influence the work reported in this paper.

Data availability

Data will be made available on request.

Acknowledgments

This work was supported by the National Natural Science Foundation of China (Grant No. 12105144), Primary Research and Development Plan of Jiangsu Province (Grant No. BE2022846, BE2023816).

References

[1] R. Cunningham, C. Zhao, N. Parab, C. Kantzos, J. Pauza, K. Fezzaa, T. Sun, A. D. Rollett, Keyhole threshold and morphology in laser melting revealed by ultrahigh-speed x-ray imaging, Science 363 (2019) 849–852, https://doi.org/10.1126/science.aav4687.

[2] N.D. Parab, J.E. Barnes, C. Zhao, R.W. Cunningham, K. Fezzaa, A.D. Rollett, T. Sun, Real time observation of binder jetting printing process using high-speed X-ray imaging, Sci. Rep. 9 (2019) 2499, https://doi.org/10.1038/s41598-019-38862-7.

[3] D.P. Finegan, M. Scheel, J.B. Robinson, B. Tjaden, I. Hunt, T.J. Mason, J. Millichamp, M. Di Michiel, G.J. Offer, G. Hinds, D.J.L. Brett, P.R. Shearing, In-operando high-speed tomography of lithium-ion batteries during thermal runaway, Nat. Commun. 6 (2015) 6924, https://doi.org/10.1038/ncomms7924.

[4] S. Miller, B. Singh, S. Cool, G. Entine, L. Campbell, R. Bishel, R. Rushing, V. V. Nagarkar, Ultrahigh-speed X-ray imaging of hypervelocity projectiles, Nucl. Instrum. Methods Phys. Res. Sect. Accel. Spectrometers Detect. Assoc. Equip. 648 (2011) S293–S296, https://doi.org/10.1016/j.nima.2010.11.048.

[5] M.P. Olbinado, X. Just, J.L. Gelet, M. Scheel, P. Vagovic, T. Sato, J. Schulz, A. Mancuso, J. Morse, A. Rack, MHz frame rate hard X-ray phase-contrast imaging using synchrotron radiation, Opt Express 25 (2017) 13857–13871, https://doi.org/10.1364/OE.25.013857.

[6] Z. Jiang, J. Wang, Research status of on-line monitoring of laser metal deposition, IOP Conf. Ser. Mater. Sci. Eng. 605 (2019) 012020, https://doi.org/10.1088/1757-899X/605/1/012020.

[7] Z.J. Hou, Q. Wang, C.G. Zhao, J. Zheng, J.M. Tian, X.H. Ge, Y.G. Liu, Online monitoring technology of metal powder bed fusion processes: a review, Materials 15 (2022) 7598, https://doi.org/10.3390/ma15217598.

[8] M.P. Olbinado, J. Grenzer, P. Pradel, T.D. Resseguier, P. Vagovic, M.C. Zdora, V. A. Guzenko, C. David, A. Rack, Advances in indirect detector systems for ultra high-speed hard X-ray imaging with synchrotron light, J. Instrum. 13 (2018), https://doi.org/10.1088/1748-0221/13/04/C04004. C04004-C04004.

[9] C. Hu, L. Zhang, R.Y. Zhu, M. Demarteau, R. Wagner, L. Xia, J. Xie, X. Li, Z. Wang, Y. Shih, T. Smith, Ultrafast inorganic scintillator-based front imager for Gigahertz Hard X-ray imaging, Nucl. Instrum. Methods Phys. Res. Sect. Accel. Spectrometers Detect. Assoc. Equip. 940 (2019) 223–229, https://doi.org/10.1016/j.nima.2019.06.011.

[10] S.L. Barna, J.A. Shepherd, M.W. Tate, R.L. Wixted, E.F. Eikenberry, S.M. Gruner, Characterization of a prototype pixel array detector (PAD) for use in microsecond framing time-resolved X-ray diffraction studies, IEEE Trans. Nucl. Sci. 44 (1997) 950–956, https://doi.org/10.1109/23.603783.

[11] H.T. Philipp, M.W. Tate, P. Purohit, K.S. Shanks, J.T. Weiss, S.M. Gruner, High-speed X-ray imaging pixel array detector for synchrotron bunch isolation, J. Synchrotron Radiat. 23 (2016) 395–403, https://doi.org/10.1107/S1600577515022754.

[12] H.T. Philipp, M.W. Tate, P. Purohit, D. Chamberlain, K.S. Shanks, J.T. Weiss, S. M. Gruner, High-speed x-ray imaging with the Keck pixel array detector (Keck PAD) for time-resolved experiments at synchrotron sources, New York, NY USA, https://doi.org/10.1063/1.4952908, 2016.

[13] D. Danopoulos, K. Anagnostopoulos, C. Kachris, D. Soudris, FPGA acceleration of generative adversarial networks for image reconstruction, in: 2021 10th Int. Conf. Mod. Circuits Syst. Technol. MOCAST, IEEE, Thessaloniki, Greece, 2021, pp. 1–5, https://doi.org/10.1109/MOCAST52088.2021.9493361.

[14] S.O. Memik, A.K. Katsaggelos, M. Sarrafzadeh, Analysis and FPGA implementation of image restoration under resource constraints, IEEE Trans. Comput. 52 (2003) 390–399, https://doi.org/10.1109/TC.2003.1183952.

[15] U. Trunk, A. Allahgholi, J. Becker, A. Delfs, R. Dinapoli, P. Göttlicher, H. Graafsma, D. Greiffenberg, H. Hirsemann, S. Jack, A. Klyuev, H. Krueger, S. Lange, T. Laurus, A. Marras, D. Mezza, A. Mozzanica, J. Poehlsen, S. Rah, B. Schmitt, J. Schwandt, I. Sheviakov, X. Shi, Q. Xia, J. Zhang, M. Zimmer, in: T.G. Etoh, H. Shiraga (Eds.), AGIPD: a Multi Megapixel, Multi Megahertz X-Ray Camera for the European XFEL, 2017 1032805, https://doi.org/10.1117/12.2269153. Osaka, Japan.

[16] F. Fahim, S. Joshi, S.O. Memik, H. Mohseni, A low-power, high-speed readout for pixel detectors based on an arbitration tree, IEEE trans. Very large scale integr, VLSI Syst 28 (2020) 576–584, https://doi.org/10.1109/TVLSI.2019.2953871.

[17] G.A. Carini, G.W. Deptuch, F. Fahim, Ł.A. Kadłubowski, P. Klabbers, S. Lauxtermann, P.-O. Petterson, T. Zimmerman, Hybridized MAPS with an in-pixel A-to-D conversion readout ASIC, Nucl. Instrum. Methods Phys. Res. Sect. Accel. Spectrometers Detect. Assoc. Equip. 935 (2019) 232–238, https://doi.org/10.1016/j.nima.2019.03.091.

[18] M.B. Valentin, G. Di Guglielmo, D. Noonan, P. Dilip, P. Huang, A. Quinn, T. Zimmerman, D. Braga, S. Ogrenci, C. Jacobsen, N. Tran, F. Fahim, In-pixel AI for lossy data compression at source for X-ray detectors, Nucl. Instrum. Methods Phys. Res. Sect. Accel. Spectrometers Detect. Assoc. Equip. 1057 (2023) 168665, https://doi.org/10.1016/j.nima.2023.168665.

[19] P. Eckert, H.-C. Schultz-Coulon, W. Shen, R. Stamen, A. Tadday, Characterisation studies of silicon photomultipliers, Nucl. Instrum. Methods Phys. Res. Sect. Accel. Spectrometers Detect. Assoc. Equip. 620 (2010) 217–226, https://doi.org/10.1016/j.nima.2010.03.169.

[20] D.P. Kingma, J. Ba, Adam: a method for stochastic optimization. http://arxiv.org/abs/1412.6980, 2017. (Accessed 4 February 2024).

[21] Z. Feng, Y. Liu, J. Mu, W. Chen, S. Lai, X. Tang, Optimization and testing of groove-shaped grid-controlled modulated X-ray tube for X-ray communication, Nucl. Instrum. Methods Phys. Res. Sect. Accel. Spectrometers Detect. Assoc. Equip. 1026 (2022) 166218, https://doi.org/10.1016/j.nima.2021.166218.

[22] L. Claus, L. Fang, R. Kay, M. Kimmel, J. Long, G. Robertson, M. Sanchez, J. Stahoviak, D. Trotter, J.L. Porter, in: J.A. Koch, G.P. Grim (Eds.), An Overview of the Ultrafast X-Ray Imager (UXI) Program at Sandia Labs, 2015, p. 95910P, https://doi.org/10.1117/12.2188336. San Diego, California, United States.